ASGE Vol. 03 (03), pp. 43-62, 2022

Egyptian Knowledge Bank

International Journal of Advances in Structural and Geotechnical Engineering

https://asge.journals.ekb.eg/

Print ISSN 2785-9509 Online ISSN 2812-5142

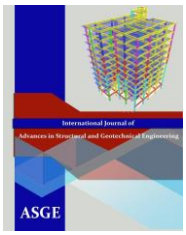

MOMENT-SHEAR INTERACTION OF HIGH-PERFORMANCE CONCRETE TWO WAY SLABS

Tarek F. El-Shafiey [1], Salah El-Din F. Taher [2], Ahmed T. Baraghith [3] and Emad El-Din M. Ogail [4]

[1] *Professor, Faculty of Engineering, Tanta University, Tanta, Egypt*
E-mail: Tarek.elshafiey@f-eng.tanta.edu.eg
[2] *Professor, Faculty of Engineering, Tanta University, Tanta, Egypt*
E-mail: Salah.taher@f-eng.tanta.edu.eg
[3] *Associate Professor, Faculty of Engineering, Tanta University, Tanta, Egypt*
E-mail: Ahmed.baraghit@f-eng.tanta.edu.eg
[4] *Assistant Lecturer, Faculty of Engineering, Tanta University, Tanta, Egypt*
E-mail: Emad.Magdi@f-eng.tanta.edu.eg

ABSTRACT

Reinforced concrete buildings are frequently exposed to seismic loadings. This condition generates either uniaxial or biaxial unbalanced moment on slab-to-column connections. The design of such connections varies greatly between most international codes. This paper investigates the effect of the unbalanced moment on the punching shear strength of two-way interior slab-to-column connections. For this purpose, a nonlinear finite element analysis using ANSYS-V19.2 software package was performed. Thirteen High-Performance Concrete (HPC) slabs with different eccentricities were analyzed. During this context, a number of three large scale specimens made of HPC were firstly tested experimentally to validate the used model. The interaction diagram between the unbalanced moment and the punching shear strength was developed and then compared against those resulted by different international codes (ACI 318-19, CSA A23.3-04, EC2-04, BS8110-97, and ECP 203-2018). The results showed that by increasing the unbalanced moment, the punching shear strength is significantly decreased and the failed surface from the column face is pulled toward the column. Moreover, the normalized moment-shear relationship showed a linear interaction diagram.

Keywords: Slabs, Punching Shear, Unbalanced moment, High-performance concrete (HPC), International Codes.

INTRODUCTION

Punching shear behavior of reinforced concrete slab-to-column connections subjected to concentric loading have been studied since the 1950s, and a large amount of experimental research is available [1–22]. Although interior slab-to-column connections design is often

Article history: Received May 2022 & Accepted July 2022
DOI: 10.21608/ASGE.2022.152830.1024

controlled by direct shear transfer, this condition should not be assumed without considering the sources of the unbalanced moment (moment transfer). The unbalanced moment can occur when the pattern loads are to be considered, when the span lengths of the adjacent bays differ, or when the slab-column frame is used to resist lateral loads.

The transference of the unbalanced moments in such connections reduces the punching strength and the international code provisions [23–27] assume that this reduction can be determined by increasing the shear stress at different control perimeters. The previous research in support of these provisions was conducted by Hanson and Hanson [28]. For interior slab-to-column connection with square column, Hanson and Hanson stated that 40% of the unbalanced moments are transferred by shear stresses and the remaining 60% are transferred by flexural stresses. Although disagreeing distribution percentages were reported by researchers including Moe [29] and ACI-ASCE Committee 326 [30], the provisions remain unchanged since the 1970s.

The effects of the unbalanced moment on slab-to-column connections have remained of interest to many researchers to this day. However, these researchers have deviated away from the common linear shear stress distribution assumptions depending of the prediction methods based on truss, beam, and membrane analogies. These methods were developed based on results of experimental tests in which specimens were subjected to combined gravity vertical loads and unbalanced moments. An extensive review exists in the literature [31– 40] shows that the experimental data available on the punching behavior of interior slab-to-column connections under eccentric loading is limited.

In recent years, there has been increased use of high-performance concrete (HPC) in flat slabs of high-rise buildings where both strength and durability are important considerations. An efficient use of high-performance concrete moving toward thinner cross section slabs. Punching shear is usually the governing failure mode for such slabs. A great effort was devoted to understand and manipulate the fundamental parameters related to shear behavior of HPC beams [41]. However, limited attention was directed to study the punching characteristics of HPC slabs.

This paper presents the results of three experimental tests carried out on large-scale two-way HPC slabs subjected to combined vertical gravity load and unbalanced moment. The behavior of these slabs is described and discussed in terms of cracking patterns, failure modes, ultimate loads toughness, and vertical displacements. Expanded finite element program was conducted to further investigate the effect of the unbalanced moment. Furthermore, the interaction diagram between vertical shear and the unbalanced moment was developed.

EXPERIMENTAL WORK

Test Specimens

Three square reinforced high-performance concrete (HPC) slabs without transverse reinforcement were cast and tested to investigate the influence of the unbalanced moment on the punching shear strength of these slabs and later to validate the numerical model that can predict the punching shear strength of such slabs. All slabs had the same thickness of 120 mm and the same dimensions of 1700 x 1700 mm with clear span 1600 for each side. The dimensions and reinforcement details of the tested slab are shown in Figs. 1 and 2. The first specimen was loaded by concentric loading applied directly on the slab through a steel plate. Both the second and third specimens were loaded by uniaxial and biaxial loading of e/t=0.83 (t= slab thickness); respectively. To generate this loading type, a column with cantilever was cast with the specimens so that the eccentricity could be created when the load is applied on the cantilever. The load was applied through a steel plate of dimensions 150 x 150 x 40 mm. The steel plate was fixed to the specimens by gypsum to assure uniform distributed pressure at the loading surface. All slab specimens had a constant flexural reinforcement ratio of 1.675 % (15 D 16 mm in both directions) arranged in the tension side only. Table 1. summarizes the main data and the slab designations for the tested specimens.

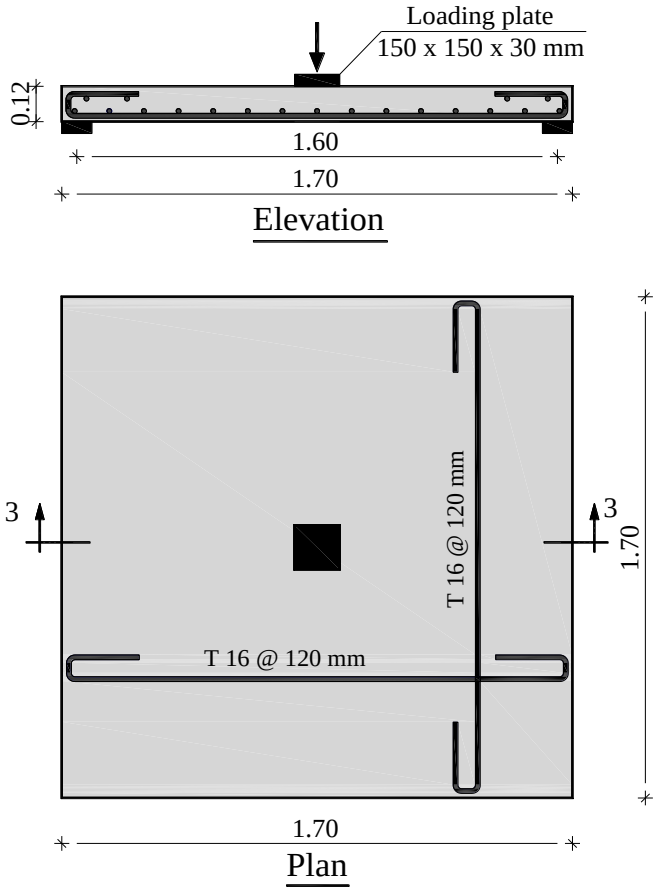

Fig. 1: Reinforcement details for specimens of concentric loading (SC-0).

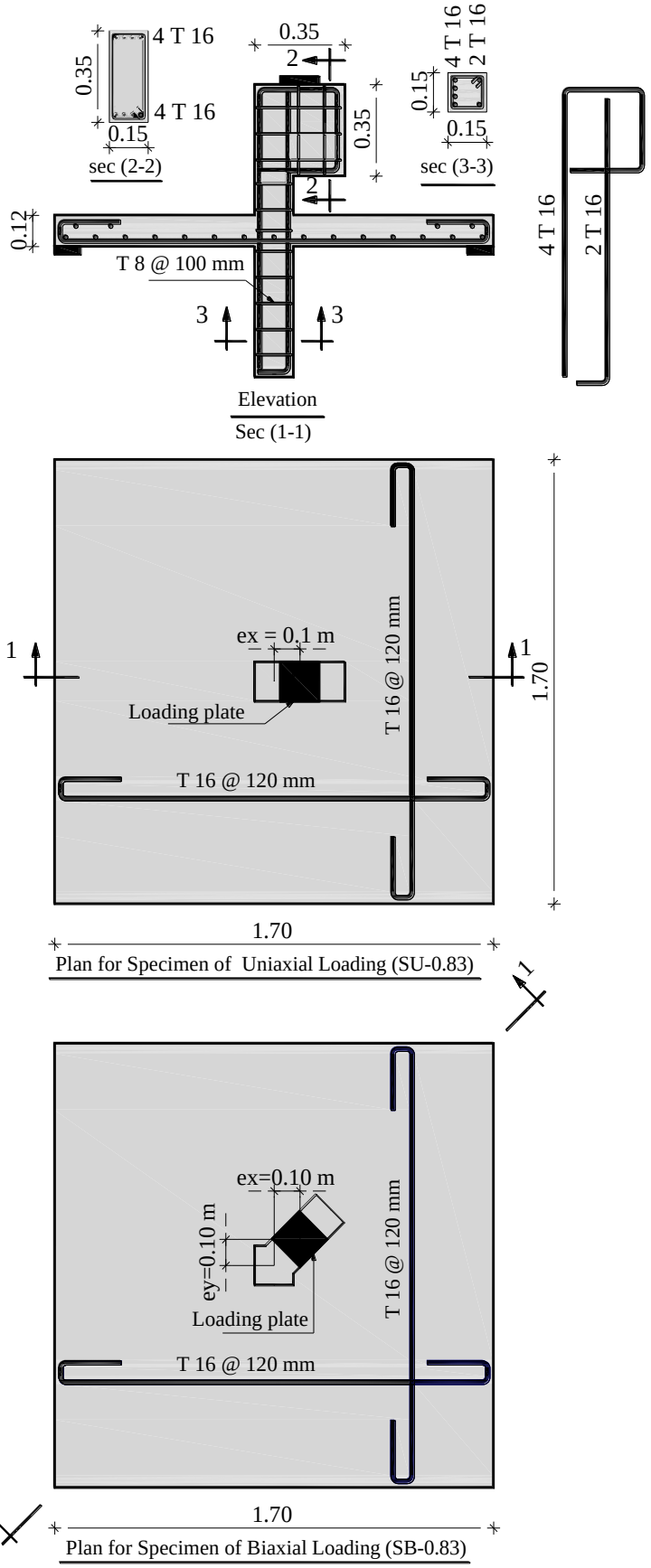

Fig. 2: Reinforcement details for specimens of uniaxial and biaxial loading.

Table 1: Test matrix.

Specimen	Loading type	Eccentricity		f_c'(MPa)	f_t (MPa)
		e_x/t	e_y/t		
SC-0	Concentric loading	0	0	60.53	6.14
SU-0.83	Uniaxial loading	0.83	0	60.21	6.05
SB-0.83	Biaxial Loading	0.83	0.83	61.02	6.34

Materials

The concrete components used in this experimental work had been found to be appropriate to produce high-performance concrete in previous investigation of Horszczaruk [42]. The mix design processes mainly the characteristics: high compressive strength, high tensile strength, ductility, and durability. The concrete was produced using 450 kg/m^3 of Portland cement CEM I 52.5R., continuously graded crushed basalt with nominal particle size of 16 mm, 535 kg/m^3 quartz sand having a fineness modulus of 2.5, and water to binder ratio of 0.3 (w/b). Silica fume containing 92% SiO_2 and having a specific surface area of 19,000 m^2/kg was added in the mixing process to enhance its mechanical properties. Polypropylene fibers of length 12 mm, diameter 25 μm, density 0.9 g/cm3, tensile strength 0.35 GPa, and modulus of elasticity 35 GPa was used with volumetric ratio to 1.0%. The concrete mixture compositions are given in Table 2. The concrete compressive (f_c'), and splitting tensile (f_t) strengths were determined on 150 × 300 mm cylinders based on the ASTM C39 [43] and ASTM C 496 [44] standard test methods; respectively. These results are summarized in Table 1. In order to determine the yield stress and the tensile strength of the longitudinal reinforcement, direct tensile tests using universal testing machine were performed on three coupons from the same steel batch and the results were 407 MPa and 611 MPa on average; respectively.

Test Setup and Instrumentation

All specimens were positioned and tested as showed in Figs. 3 and 4. The boundary conditions of the specimens were simply supported on the four edges. Test specimens were instrumented to measure the applied load, central deflection, and reinforcement strains. The central deflection of the slabs was measured using a linear variable differential transformer (LVDT) gauges with a length of 100 mm. The developed tensile normal strain on the steel bars was measured by an electrical strain gauge of 6 mm length positioned at the maximum stressed section at the edge of the loading steel plate. The slabs were loaded incrementally considering the load control scheme in several steps at a loading rate ranged from 0.1 to 0.2 kN/s up to failure.

Table 2: Concrete mix proportions.

Cement (kg/m3)	Coarse aggregate (kg/m3)	Fine aggregate (kg/m3)	W/B*	Silica fume (kg/m3)	Super-plasticizer (kg/m3)	Fiber volumetric ratio (%)
450	1279	535	0.3	45	4.5	1

* W/B is the water/ binder ratio, B = cement + silica fume

Fig. 3: Test setup for specimen with concentric loading.

a- Specimen SU-0.83

b- Specimen SB-0.83

Fig. 4: Test setup for specimens with eccentric loading.

The acting load was measured by a load cell of 1000 kN capacity. After each loading step, the vertical central deflection and the developed normal strains in the longitudinal steel bars were recorded and stored using an automatic data logger unit (TDS-150).

EXPERIMENTAL RESULTS

The exhibited modes of failure, the cracking and ultimate loads, deflection behavior, and steel strains are selectively considered and compared for test specimens. Table 3. summarizes the main results obtained from experimental work.

Table 3: Main results obtained from experimental work.

Specimen	Loading type	Eccentricity		V_u (kN)	Max. deflection (mm)	M_x (kN.m)	M_y (kN.m)	$M' = \sqrt{{M_x}^2 + {M_y}^2}$
		e_x/t	e_y/t					
SC-0	Concentric loading	0	0	396	9.01	0	0	0
SU-0.83	Uniaxial loading	0.83	0	324	8.04	32.4	0	32.4
SB-0.83	Biaxial Loading	0.83	0.83	298	8.0	29.8	29.8	42.14

Crack Pattern and Modes of Failure

Fig. 5 shows the observed final crack patterns at the bottom surface for the tested specimens. The flexural cracks initiated radially around the loading area in the three specimens. With further loading, significant difference in performance was related to the flexural cracks' propagation. Crack propagation in specimen SC-0 with concentric loading was toward the corners of the slab with an approximate uniform distribution on the four corners of the slab. On the other hand, for specimen SU-0.83 with uniaxial loading, the density of the flexural cracks was much greater in the half side subjected to the compression force due to the unbalanced moment. For specimen SB-0.83 with biaxial loading, more flexural cracks were propagated toward only one corner that represents the compression force resulted from the biaxial unbalanced moment. By reaching the ultimate load, a sudden penetration of the slab top layer occurred beneath the applied load. The failure mode of all specimens was punching failure with top penetration of the load and with occurrence of tangential cracks in the bottom fiber of the slabs. For all tested specimens, the main steel strain did not reach yield. The failed surface had almost complete circle in specimen SC-0, while the failed surface was about half circle and quarter circle in specimens SU-0.83 and SB-0.83; respectively. That's because the unbalanced moment exerts additional punching stresses in the compression side. The distance from the outer edge of the failed surface to the column face was about 3.0 d for specimen SC-0.83, while the distance was about only 1.6d for both specimens SU-0.83 and SB-0.83 (where d is the effective depth of the slab and equals 100 mm). This means that, the unbalanced moment works on pulling the critical shear crack toward the loading area.

Cracking and Ultimate Loads

The test result of first flexural cracking and the ultimate load just before failure for all specimens are illustrated graphically in Fig. 6. Applying additional shear stresses due to the unbalanced moment, led to a significant decrease in flexural cracking and ultimate loads of the specimens. Specimen of uniaxial loading SU-0.83 decreased by about 25.9% and 18.2 % in the terms of flexural cracking load and ultimate load; respectively, as compared to specimen of concentric loading SC-0. Specimen SB-0.83 of biaxial loading decreased by about 31.8 % and 24.8 % in the same terms.

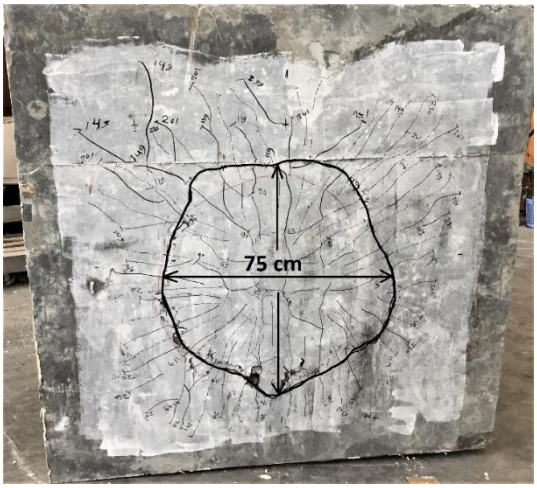

Specimen SC-0 (Exp.)

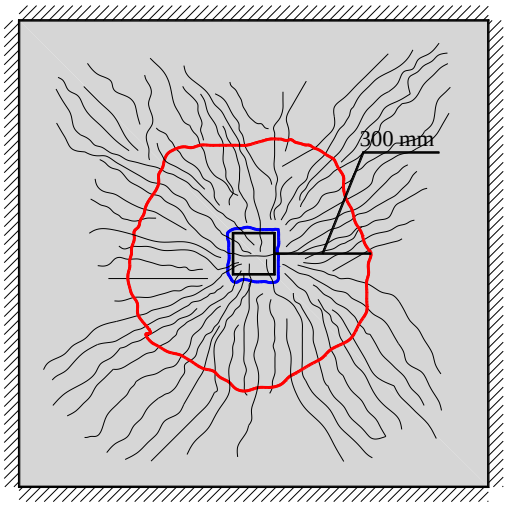

Specimen SC-0 (Sketch)

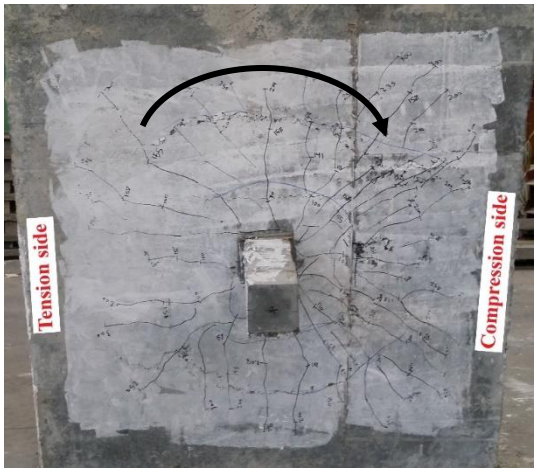

Specimen SU-0.83 (Exp.)

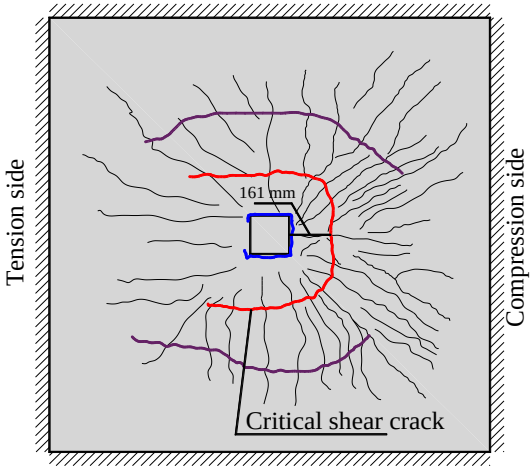

Specimen SU-0.83 (Sketch)

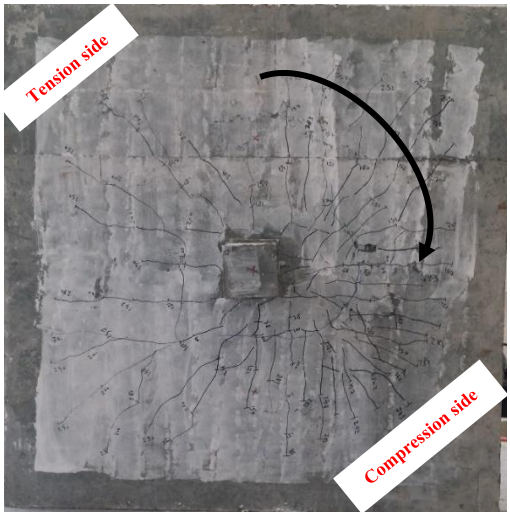

Specimen SB-0.83 (Exp.)

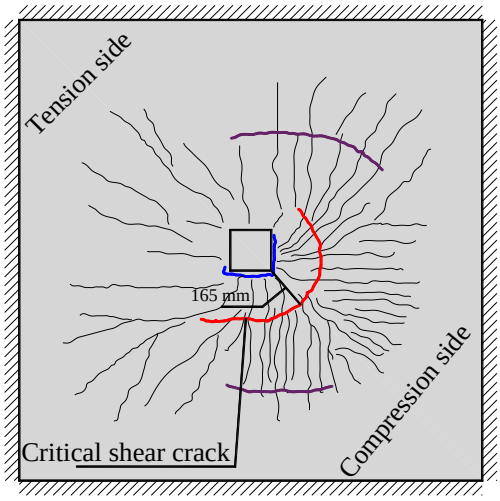

Specimen SB-0.83 (Sketch)

Fig. 5: Crack patterns after failure at bottom surface of all tested Specimens.

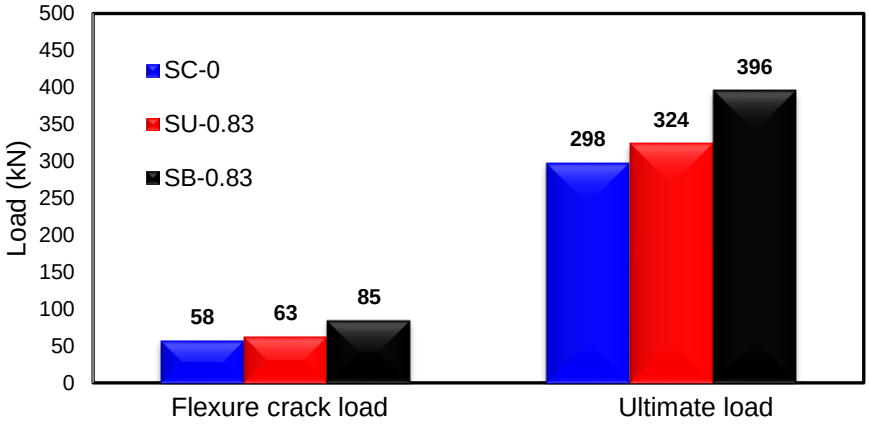

Fig. 6: Cracking and ultimate load for all tested specimens.

Load-deflection Behavior

The load-deflection behavior of the tested HPC specimens is shown in Fig. 7. In general, it can be observed that the load-deflection for all slabs can be divided into two stages. The first stage from zero loading up to the ultimate load (Pre-Peak stage). In this stage the load-deflection behavior can be represented by bilinear behavior bounded by cracking point and ultimate point. The second stage starts just after reaching the ultimate load (Post- Peak stage). The upper loading steel plate penetrated the top fiber of the specimen causing a sudden drop of the load to a certain value, then an approximate horizontal plateau was occurred representing the residual load of the specimen. The residual load may be due to the membrane action of the longitudinal steel and the remaining tension strength of concrete. For the considered specimen, the applied moment decreased the stiffness of the specimens by about 5.9 % and 19.3 % for specimens SU-0.83 and SB-0.83; respectively. The maximum central deflections just before punching failure for specimens SC-0, SB-0.83 and SB-0.83 were 9.03 mm, 8.04 mm, and 8.0 mm; respectively.

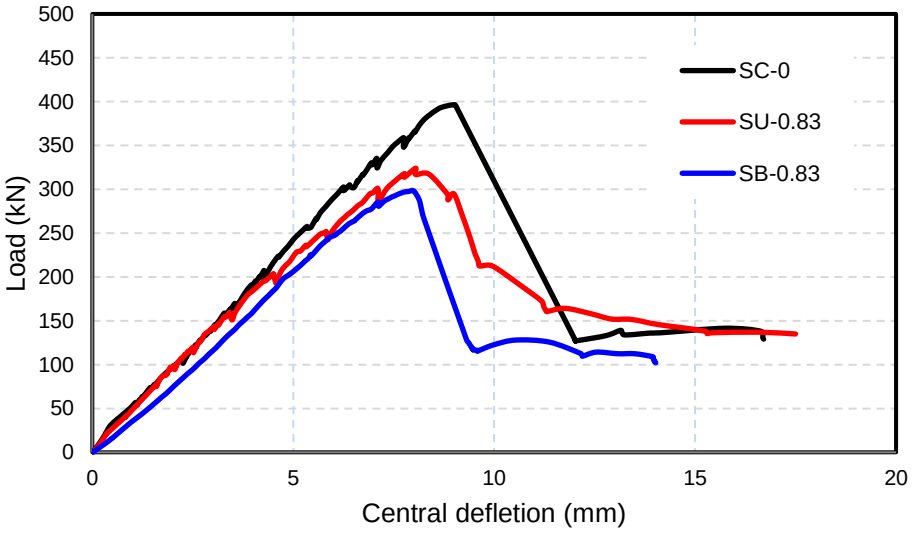

Fig. 7: Load-central deflection for all tested specimens.

Toughness

Toughness (energy absorption capacity) is usually defined as the area under the load-deflection curve up to the ultimate load. However, to make the best use of the total load-deflection curve this area was taken up to the point of residual strength as seen in Fig. 8. The residual strength was existing in the load - deflection curves for most pervious researchers such as Ruiz, et al . [٤٥]. The difference among the tested specimens can be shown in Fig. 9. It can be noticed that applying unbalanced moments lead to a decrease in the energy absorption capacity for specimens failed in punching shear. This means that the failure become more brittle and catastrophic.

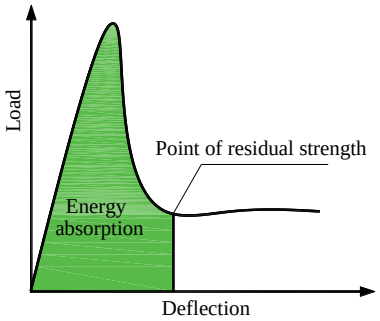

Fig. 8: Definition of the energy absorbed and the point of the residual strength

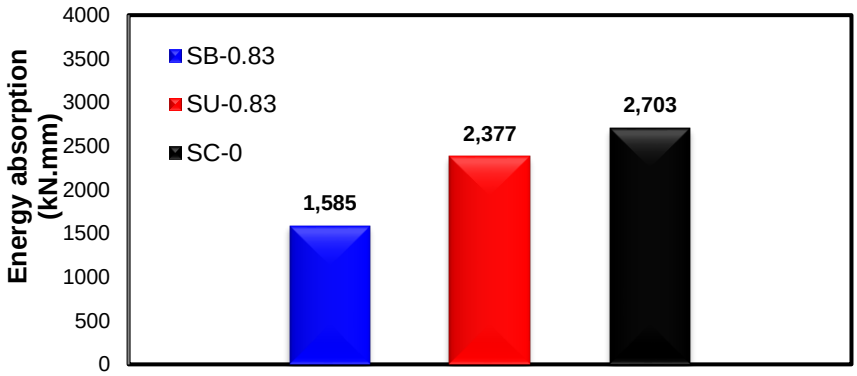

Fig. 9: Energy absorption bar chart for all tested specimens.

FINITE ELEMENT SIMULATIONS

A numerical analysis using ANSYS-V19.٢ finite element package had been performed. The applied load was iterated step by step using the Newton-Raphson method.

Modeling of Concrete

The eight-nodded brick element SOLID65 was used to model the HPC concrete. This element has three degrees of freedom at each node translation in the nodal x, y and z directions. The element has the capability of plastic deformation, cracking in three orthogonal directions and crushing [٤٦]. A schematic of the element was shown in Fig. 10-a. In the element formulation, the multi-linear isotropic material uses von Mises failure criterion along with the William and

Warnke [٤٧] model to define the failure of the concrete. The compressive uniaxial stress-strain relation of concrete model is assumed according ACI 318 – 19 [٢٣] code equations as following:

$$f = \frac{E_c \varepsilon}{1 + \left(\frac{\varepsilon}{\varepsilon_o}\right)^2} \quad (MPa) \qquad (1)$$

$$\varepsilon_o = \frac{2f_c'}{E_c} \quad (MPa) \qquad (2)$$

$$E_c = 3320\sqrt{f_c'} + 6900 \quad (MPa) \qquad (3)$$

Where the stress f at any is strain ε in MPa and ε_o is the strain corresponding to the peak stress, and E_c is the young modulus calculated for high strength concrete according to ACI 318-19 [٢٣]. The uniaxial tensile cracking stress, was taken from the experimental results for each specimen. Polypropylene fibers (PP fibers) were modeled as smeared rebars in SOLID65 element uniformly distributed in the three orthogonal directions. Preliminary trials were carried out to determine the shear transfer coefficients and the tension stiffening factor in case of the fibers presence and were found 0.7 for shear transfer coefficient for an open crack (β_t), 1.0 for shear transfer coefficients for a closed crack (β_c) and 1.0 for the tension stiffening factor.

Modeling of Reinforcement Bars and Loading Plate

Reinforcement was always modeled by link elements or being smeared in concrete element ignoring the dowel action effects of the reinforcement [٤٦]. In this study, the reinforcement was modeled by a solid element to consider the dowel action effect. SOLID185 element was used to model the reinforcement and the loading plates. The element is defined by eight nodes having three degrees of freedom at each node translation in the nodal x, y and z directions. The element has plasticity, stress stiffening, large deflection, and large stain capabilities [٤٦]. A schematic of the element was shown in Fig. 10-b. Bilinear isotropic idealization for the reinforcement was adopted with the tangent modulus where is the young modulus of steel. The bond between concrete and reinforcement was assumed to be perfect. Steel plates were used at the load locations in the finite element models to provide a more even stress distribution over the load areas. SOLID 185 element is also used to model the steel plates. An elastic modulus equal to 200,000 MPa and Poisson's ratio of 0.3 were used for the plates. The steel plates were assumed to be linear elastic materials.

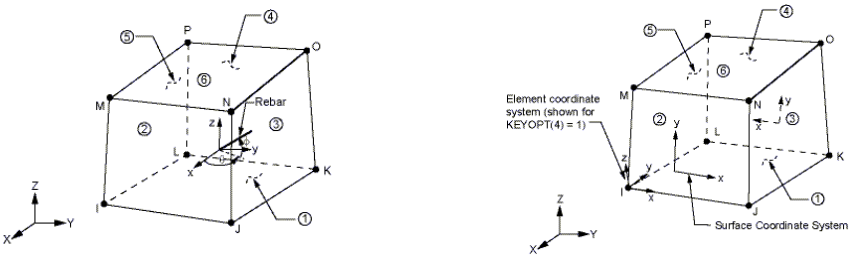

a) SOLID 65 element b) SOLID 185 element

Fig.10: 3D solid elements used in the study.

Geometry and Meshing

Fig. 11 presents the 3d non-linear finite element mesh for the used model. The numerical specimens were high performance reinforced concrete slabs of mm dimensions and loading steel plate of mm. For simplicity, the load was applied on a column with double cantilevers, so that the eccentricity in both directions could be simulated when needed. The column was modeled by using the concrete solid element SOLID65 having the uniaxial compressive strength (f_c') and uniaxial tensile strength (f_t) equal toto have enough rigidity to prevent the cracking and the crushing of the concrete [46], which ensures that, the failure is occurred only in the slab.

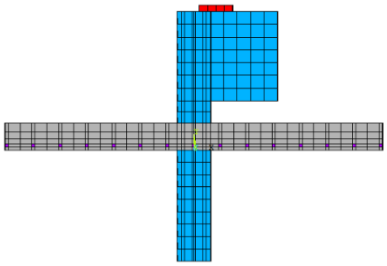

a- Elevation view

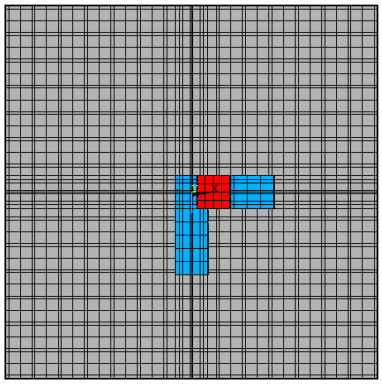

b- Top view

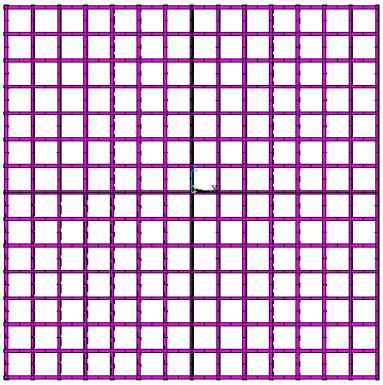

c- Reinforcement mesh (SOLID185)

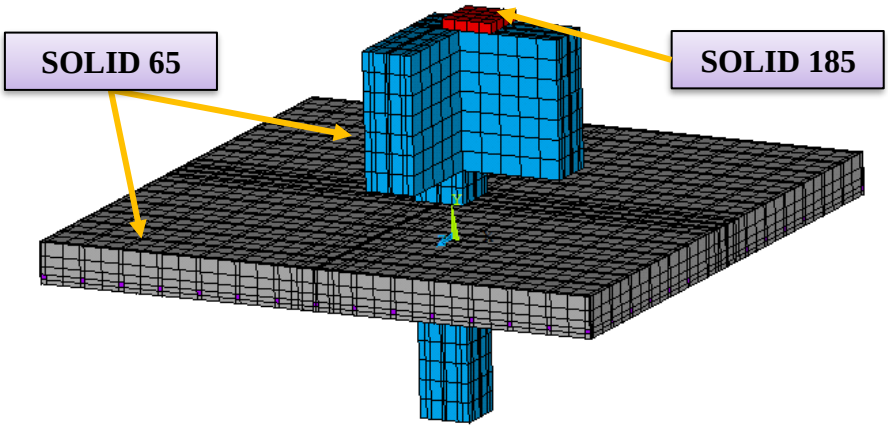

a- Isometric view

Fig. 11: Geometry and meshing of the used model.

VERIFICATION AGAINST EXPERIMENTAL WORK

The comparison between numerical model and the experimental tests is presented in Table 4 as well as Figs. 12 and 13. In general, all numerical models have accurately predicted the ultimate load and represented well the nonlinear load-deflection response up to the ultimate load. The numerical load-deflection curves are slightly stiffer than the experimental curves. The observed failure modes on the experimental tests were successfully predicted as given by the experimental test specimens.

Table 4: Comparison between experimental tests and finite element results in terms of flexural cracking and ultimate loads.

Specimen	Finite element prediction		Experimental tests		Ratio	
	V_{cr} (kN)	V_u (kN)	V_{cr} (kN)	V_u (kN)	$\frac{V_{cr,FE}}{V_{cr,EXP}}$	$\frac{V_{u,FE}}{V_{u,EXP}}$
SC-0	77	411	85	396	0.90	1.04
SU-0.83	70	330	63	324	1.11	1.02
SB-0.83	62	293	58	298	1.06	0.98
Average					1.085	1.013
Standard deviation					0.025	0.025
Coefficient of variance (COV)					0.023	0.025

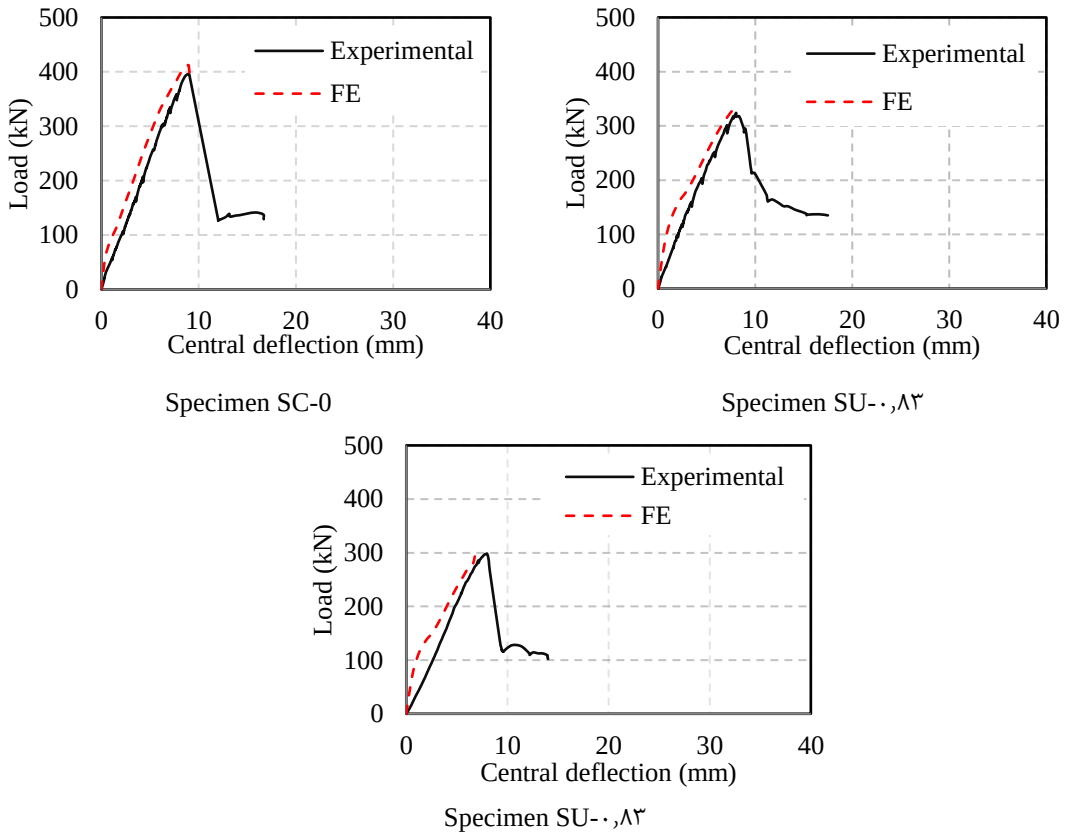

Specimen SC-0 Specimen SU-٠,٨٣

Specimen SU-٠,٨٣

Fig. 12: Load-deflection verification of the 3-D FE model.

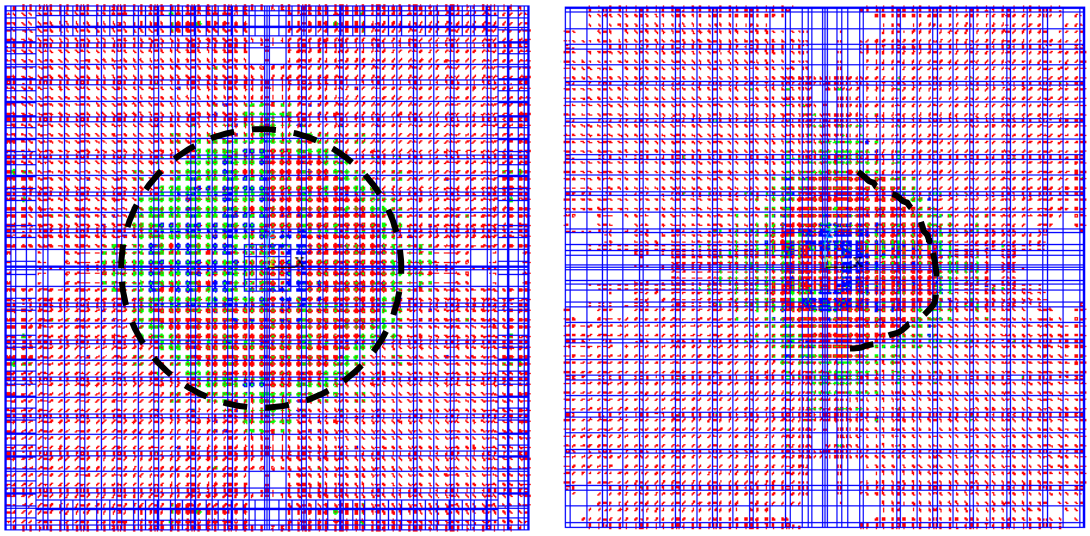

Specimen SC-0 Specimen SU-٠,٨٣

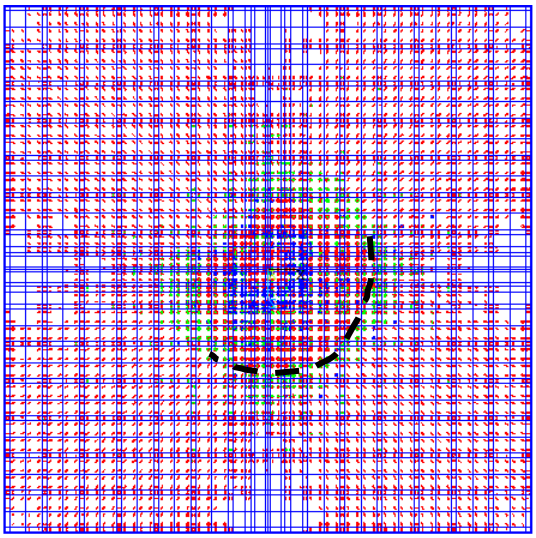

Specimen SU-٠,٨٣

Fig. 13: Crack pattern verification of the 3-D FE model (Bottom view).

EFFECT OF THE UNBALANCED MOMENT ON PUNCHING STRENGTH

In order to further investigate the influence of the unbalanced moment on the punching shear capacity of HPC slabs, a series of specimens with different load eccentrics for either uniaxial and biaxial loading were considered and conducted by the numerical model. Table 5 shows the considered specimen and the results. The presence of the unbalanced moment in the slab-column connection significantly reduces the punching load capacity of the slab. This can be observed also in the load-deflection curves as shown in Figs. 14 and 15. For the uniaxial loading, the reduction of the punching capacity for the specimen of e/t=2.5 was about 44 % as compared to the specimen of concentric loading. For the biaxial loading, the reduction was about 56 % for the same specimen. This means that applying the unbalanced moment in both directions had a significant decrease on the punching capacity. Increasing the unbalanced

moment value increases the intensity of cracks at the same loading level and reduces the slab stiffness.

Table 5: Summary of the results for all finite element case studies.

Loading type	Eccentricity		V_u (kN)	Max. deflection (mm)	M_x (kN.m)	M_y (kN.m)	$M' = \sqrt{M_x^2 + M_y^2}$
	e_x/t	e_y/t					
Concentric loading	0	0	405	7.8	0	0	0
Uniaxial loading	0.42	0	367	8.09	18.35	0	18.35
	0.83	0	330	8.34	33	0	33
	1.25	0	297	7.50	44.55	0	44.55
	1.67	0	269	7.44	53.8	0	53.8
	2.08	0	248	6.76	62	0	62
	2.5	0	230	6.60	69	0	69
Biaxial Loading	0.42	0.42	330	7.68	16.5	16.5	23.33
	0.83	0.83	293	6.76	29.3	29.3	41.44
	1.25	1.25	245	5.85	36.75	36.75	52.04
	1.67	1.67	218	5.36	43.6	43.6	61.66
	2.08	2.08	198	5.32	49.50	49.50	70.00
	2.5	2.5	178	5.02	53.4	53.4	75.52

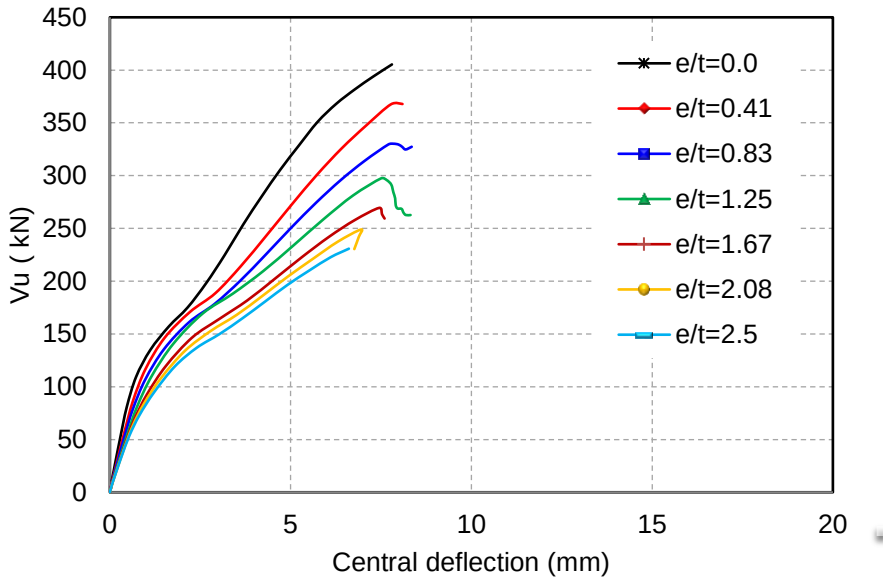

Fig. 14: Load- central deflection curves for HPC specimens of uniaxial loading.

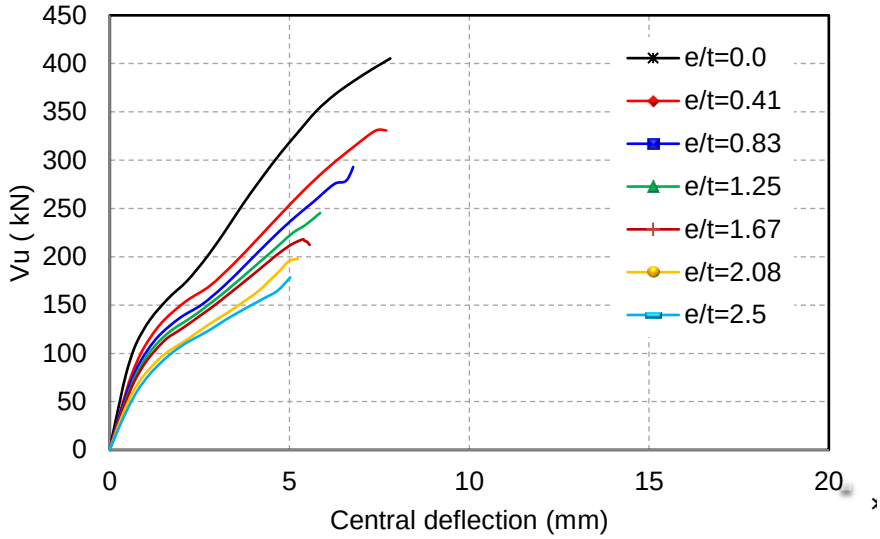

Fig. 15: Load- central deflection curves for HPC specimens of biaxial loading.

MOMENT-SHEAR INTERACTION DIAGRAM

The interaction diagrams between the punching load and the unbalanced moment for uniaxial and biaxial loading were developed as seen in Figs. 16 and 17. The interaction diagram showed approximately linear relationship for both uniaxial and biaxial loading. All considered codes equations had also a linear interaction diagram with conservative results for HPC slabs. It worth mentioning that, the British standard code equation BS8110-97 is the least conservative one.

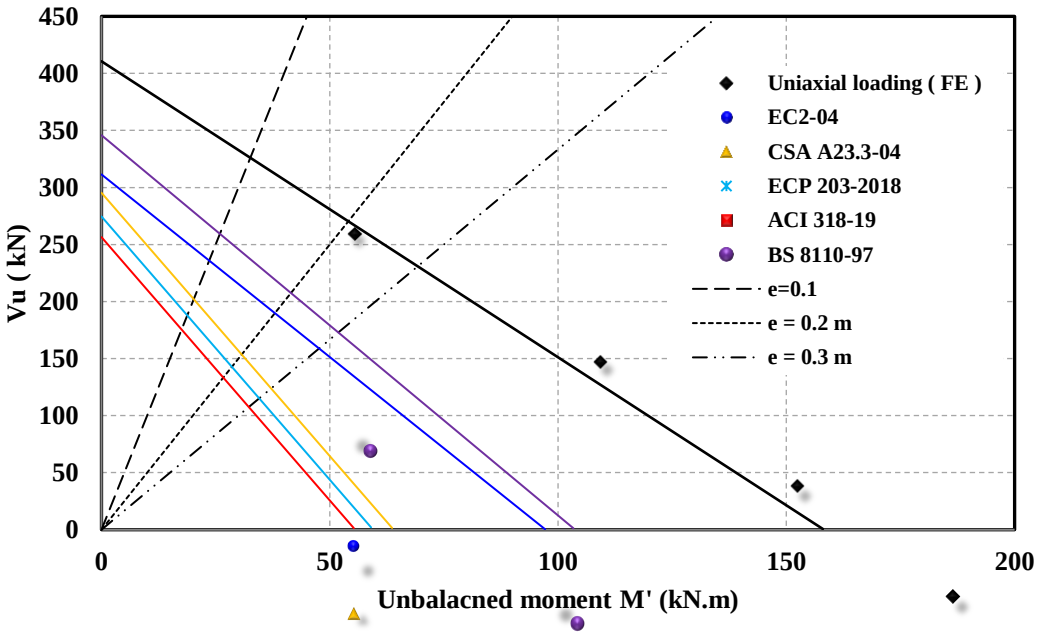

Fig. 16: Interaction diagram between the punching shearing load and the unbalanced moment (Uniaxial loading).

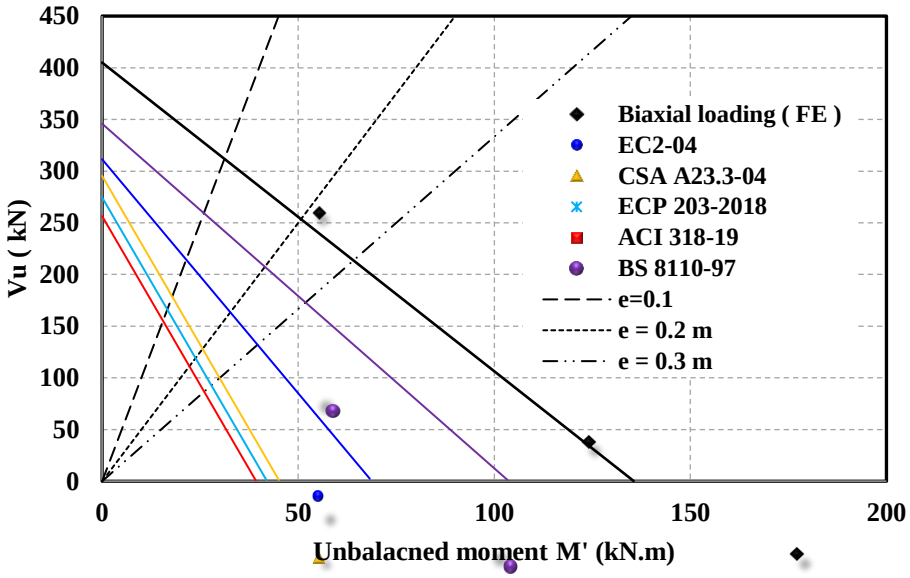

Fig. 17: Interaction diagram between the punching shearing load and the unbalanced moment (Biaxial loading).

CONCLUSIONS

In the current study, the effects of unbalanced moment (Uniaxial or biaxial) on the punching capacity of high-performance concrete (HPC) slabs have been investigated. Based on the geometry of the tested slabs, the following conclusions are drawn:

1. The existence of the unbalanced moment has a significant reduction on the punching capacity of HPC slabs. The punching capacity was reduced by about 43 % and 57 % for e/t=2.5 for uniaxial loading and biaxial loading; respectively.
2. The unbalanced moment works on pulling the critical shear crack toward the loading area, and hence the punching resistance is reduced.
3. Increasing the unbalanced moment value increases the intensity of cracks at the same loading level and reduces the slab stiffness.
4. Unbalanced moments lead to decrease in the energy absorption capacity for specimens failed in punching shear.
5. The mathematical manipulation of the trend for the interaction between the punching capacity and the unbalanced moment yielded best fit regression linear form.

Acknowledgements

Thanks are due to the team of the Reinforced Concrete and Heavy Structures Laboratory at the Faculty of Engineering, Tanta University.

REFERENCES

1. Deifalla, A. (2021). A mechanical model for concrete slabs subjected to combined punching shear and in-plane tensile forces. *Engineering Structures*, *231*, 111787.
2. Milligan, G.J., Polak, M.A., Zurell, C. (2020).Finite element analysis of punching shear behaviour of concrete slabs supported on rectangular columns. Engineering Structures,224
3. Schmidt, P., Kueres, D., Hegger, J. (2020). Punching shear behavior of reinforced concrete flat slabs with a varying amount of shear reinforcement. Structural Concrete,21(1) 235-246
4. Inácio, M.M.G., Lapi, M., Pinho Ramos, A. (2020). Punching of reinforced concrete flat slabs – Rational use of high strength concrete. Engineering Structures,206
5. Deifalla, A. (2020). Strength and ductility of lightweight reinforced concrete slabs under punching shear. Structures,272329-2345
6. Setiawan, A., Vollum, R.L., Macorini, L. (2020). Punching shear design of RC flat slabs supported on wall corners. Structural Concrete,21(3) 859-874
7. Kinnunen S, Nylander H. Punching of concrete slabs without shear reinforcement. Transactions of the Royal Institute of Technology Stockholm, Sweden. 1960. p. 112p.
8. Regan PE. Symmetric punching of reinforced concrete slabs. Mag Concr Res 1986. https://doi.org/10.1680/macr.1986.38.136.115.
9. Broms CE. Shear reinforcement for deflection ductility of flat plates. ACI Struct J 1990. https://doi.org/10.14359/2988.
10. [Marzouk H, Hussein A. Experimental investigation on the behavior of high-strength concrete slabs. ACI Struct J 1992. https://doi.org/10.14359/1261.
11. Yamada T, Nanni A, Endo K. Punching shear resistance of flat slabs: Influence of reinforcement type and ratio. ACI Struct J 1992. https://doi.org/10.14359/2984.
12. Gomes R, Regan PE. Punching strength of slabs reinforced for shear with offcuts of rolled steel I-section beams. Mag Concrete Res 1999. https://doi.org/10.1680/ macr.1999.51.2.121.
13. Birkle G, Dilger WH. Influence of slab thickness on punching shear strength. ACI Struct J 2008. https://doi.org/10.14359/19733.
14. Guandalini S, Burdet OL, Muttoni A. Punching tests of slabs with low reinforcement ratios. ACI Struct J 2009. https://doi.org/10.14359/56287.
15. Lips S, Ruiz MF, Muttoni A. Experimental investigation on punching strength and deformation capacity of shear-reinforced slabs. ACI Struct J 2012. https://doi.org/ 10.14359/51684132.
16. Ferreira MP, Melo GS, Regan PE, Vollum RL. Punching of reinforced concrete flat slabs with double-headed shear reinforcement. ACI Struct J 2014. https://doi.org/ 10.14359/51686535.
17. Kueres D, Ricker M, Classen M, Hegger J. Fracture kinematics of reinforced concrete slabs failing in punching. Eng Struct 2018. https://doi.org/10.1016/j.engstruct.2018.05.012.

18. Kueres D, Hegger J. Two-parameter kinematic theory for punching shear in reinforced concrete slabs without shear reinforcement. Eng Struct 2018;175:201–16. https://doi.org/10.1016/j.engstruct.2018.08.023.
19. Kueres D, Schmidt P, Hegger J. Two-parameter kinematic theory for punching shear in reinforced concrete slabs with shear reinforcement. Eng Struct 2019. https://doi.org/10.1016/j.engstruct.2018.12.013.
20. Einpaul J, Fernandez Ruiz M, Muttoni A. Measurements of internal cracking in punching test slabs without shear reinforcement. Mag Concr Res 2017. https://doi.org/10.1680/jmacr.16.00099.
21. Muttoni A, Fernandez Ruiz M, Simoes JT. The theoretical principles of the critical shear crack theory for punching shear failures and derivation of consistent closedform design expressions. Struct Concr 2018. https://doi.org/10.1002/suco. 201700088.
22. Simoes JT, Fernandez Ruiz M, Muttoni A. Validation of the critical shear crack theory for punching of slabs without transverse reinforcement by means of a refined mechanical model. Struct Concr 2018. https://doi.org/10.1002/suco.201700280.
23. ACI Committee 318, 2019, Building Code Requirements for Structural Concrete (ACI 318-19) and Commentary (ACI 318R-19). American Concrete Institute, Farmington Hills.
24. Canadian Standard, 2004, Association CSA23.3, Design of concrete structures, Canadian Standard Assoc.
25. EN 1992-1-1, 2004, Eurocode 2: Design of Concrete Structures, Part 1-1, General Rules and Rules for Buildings, European Committee for Standardization, Brussels, Belgium.
26. BS 8110, 1997, Structural Use of Concrete—Part 1: Code of Practice for Design and Construction. British Standards Institution, London.
27. Egyptian code for design and construction of reinforced concrete structures (ECP 203–2018), 2018.
28. Hanson NW, Hanson JN. Shear and moment transfer between concrete slabs and columns. J PCA Res Develop Lab 1968; 10:2–16.
29. Moe J. Shearing strength of reinforced concrete slabs and footings under concentrated loads. development department Bulletin D47. Portland Cement Assoc 1961:130p.
30. ACI-ASCE Committee 326. (1962). Shear and diagonal tension: Part 3—slabs and footings. Journal of American Concrete Institute, 59(3), 353–396.
31. Anis NA. Shear strength of reinforced concrete flat slabs without shear reinforcement. London: Imperial College; 1970. p. 264p. PhD Thesis.
32. Narasimhan N. Shear reinforcement in reinforced concrete column heads. London: University of London; 1971. p. 267p. PhD thesis.
33. Stamenkovic A, Chapman JC. Local strength at column heads in flat slabs subjected to combined vertical and horizontal loading. Proc Inst Civ Eng 1974. https://doi.org/10.1680/iicep.1974.4054.

34. Regan PE. Behavior of reinforced concrete flat slabs. Construction Industry Research and Information Association (CIRIA), Report 89 London. 1981. p. 89p.
35. Elgabry AA, Ghali A. Tests on concrete slab-column connections with stud-shear reinforcement subjected to shear-moment transfer. ACI Struct J 1987.
36. Hawkins NM, Bao A, Yamazaki J. Moment transfer from concrete slabs to columns. ACI Struct J 1989. [31] Kamaraldin K. Punching shear and moment transfer in reinforced concrete flat slabs. Polytechnic of Central London; 1990. p. 278p. PhD thesis.
37. Marzouk H, Emam M, Hilal Sameh M. Effect of high-strength concrete columns on the behavior of slab-column connections. ACI Struct J 1996.
38. Marzouk H, Emam M, Hilal MS. Effect of high-strength concrete slab on the behavior of slab-column connections. ACI Struct J 1998. https://doi.org/10.14359/ 541.
39. Kruger G, Burdet O, Favre R. Punching strength of R.C. flat slabs with moment transfer. International Workshop on Punching Shear Capacity of RC Slabs. Royal Institute of Technology, TRITA-BKN Bulletin 57, Stockholm. 2000. p. 333–41.
40. Stein T, Ghali A, Dilger W. Distinction between punching and flexural failure modes of flat plates. ACI Struct J 2007.
41. A. A. Khalil, T. F. EL-Shafiey, M. Hussein, and A. T. Baraghith, "Shear behaviour of high performance reinforced concrete beams", Proceedings of the eighth Alexandria international conference on Structural and Geotechnical Engineering, AICSGE8, Department of Structural Engineering, Faculty of Engineering, Alexandria University, Alexandria, Egypt, 14-16 April 2014.
42. Horszczaruk E. K., 2009, “Hydro-Abrasive Erosion of High-Performance Fiber Reinforced Concrete”, Journal of the Science and Technology of Friction Lubrication and Wear, pp. 110 – 115.
43. ASTM C39 / C39M .Standard Test Method for Compressive Strength of Cylindrical Concrete Specimens
44. ASTM C496 / C496M. Standard Test Method for Splitting Tensile Strength of Cylindrical Concrete Specimens
45. Ruiz F. M., Mirzaei Y., Muttoni A., 2013, "Post-Punching Behavior of Flat Slabs." ACI Structural Journal, V. 110, USA, pp. 801-812.
46. ANSYS, ANSYS User’s Manual Revision 19.2, ANSYS. Inc,. United States, 2019.
47. William K. J., Warnke E. P., 1975, “Constitutive Model for the Triaxial Behavior of Concrete.” Proceedings, International Association for Bridge and Structural Engineering, Vol. 19, ISMES, Bergamo, Italy, pp. 174.